Phase ordering, transformation, and grain growth of two-dimensional binary colloidal crystals: A phase field crystal modeling

Doaa Taha,[1] S. R. Dlamini,[1] S. K. Mkhonta,[2] K. R. Elder,[3] and Zhi-Feng Huang[1]

[1]*Department of Physics and Astronomy, Wayne State University, Detroit, Michigan 48201, USA*
[2]*Department of Physics, University of Eswatini, Kwaluseni M201, Eswatini*
[3]*Department of Physics, Oakland University, Rochester, Michigan 48309, USA*

The formation and dynamics of a wide variety of binary two-dimensional ordered structures and superlattices are investigated through a phase field crystal model with sublattice ordering. Various types of binary ordered phases, the phase diagrams, and the grain growth dynamics and structural transformation processes, including the emergence of topological defects, are examined. The results are compared to the ordering and assembly of two-component colloidal systems. Two factors governing the binary phase ordering are identified, namely the coupling and competition between the length scales of two sublattices, and the selection of average particle densities of two components. The control and variation of these two factors lead to the prediction of various complex binary ordered patterns, with different types of sublattice ordering for integer versus noninteger ratios of sublattice length scales. These findings will enable further systematic studies of complex ordering and assembly processes of binary systems, particularly binary colloidal crystals.

I. INTRODUCTION

The assembly of binary colloidal crystals (BiCCs) with sublattice ordering has been of significant interest in various aspects of fundamental research and applications [1–8]. These artificial ordered systems can be synthesized from diverse types of building components that vary in size and shape and are selected or tailored to possess specific functionalities [4,5]. Variations of spatial arrangement, shape, and size of structural components translate into different macroscopic properties of the system and the fabrication of the corresponding functional materials (e.g., photonics [9] and semiconductors [10,11]), in addition to biological applications (e.g., cell culture substrates [12,13] and MRI contrast agents [14]). Although a great deal of effort has been placed on the synthesis of colloidal systems from self-assembly or directed assembly of colloidal particles or building blocks, it still remains a challenging task to precisely control and predict the structural and dynamic properties of the system. Many system parameters and growth or processing conditions, such as entropy [15], temperature [16], external magnetic or electric fields [2,17], isotropic and anisotropic interparticle interactions, and system elasticity and plasticity, determine the structural diversity of the assembly.

One of the key challenges for understanding the complex phenomena associated with colloid assembly is the development of theoretical approaches that can efficiently model nonequilibrium phenomena with multiple length scales and diffusive time scales for large enough systems of experimental relevance. Various theoretical methods have been developed to study binary colloidal structures and the associated phenomena. For example, Monte Carlo (MC) simulations have been conducted to examine the structure factor of charged binary colloidal mixtures [18] as well as the phase transformation in a two-dimensional (2D) BiCC monolayer that is consistent with experiments [19]. Similarly, molecular dynamics (MD) simulations have predicted that 2D BiCCs can only be achieved for certain particle ratios [20]. However, the system size and time range are usually limited in these atomistic simulations, given the large computational demands to access large-scale behaviors of the system.

Recently, progress has been made to overcome these limitations by the development of multiple scale approaches. Among them is the phase field crystal (PFC) method [21], which introduces crystalline ordering into the traditional phase-field-type continuum approach. PFC models, motivated from the classical density functional theory (DFT) of freezing [22,23], incorporate the small length scales of crystalline materials (including the basic features of the crystalline state such as elasticity, plasticity, defects, and multiple crystal orientations) on diffusive time scales. The system evolution is governed by dissipative and relaxational dynamics driven by free-energy minimization. This method thus bridges the gap between continuum modeling that describes the long-wavelength behavior of the system but not crystalline details, and atomistic modeling that captures the microscopic details but is computationally challenging for large systems. It has been successfully applied to the study of a broad range of phenomena such as quantum dot growth during epitaxy [24], grain boundaries of 2D materials [25,26], graphene Moiré patterns [27], colloidal solidification and growth [28,29], structural phase transformation [30,31], glass formation [32], and quasicrystal growth [33], among many others. For the application of the PFC method to colloidal systems, most existing studies are limited to the single-component crystallization process [28,29], while the study of binary colloidal structures is still lacking.

In this paper, we extend the PFC method to study various types of binary 2D colloidal structures with sublattice ordering, based on a binary PFC model developed in our prior work [26]. We start by deriving the model from classical DFT for a two-component system, keeping only two- and three-point interparticle direct correlations. The ordered structures of BiCC are found to be determined by the coupling between different sublattice length scales, as well as the average density variations of the particle species. For equal sublattice length scales we identify seven binary phases, with results consistent with recent experimental findings [1–3,8,19,34]. Using analytic and numerical methods, the stability of various phases and the coexistence between them are determined and used to construct phase diagrams. In addition, numerical simulations are employed to examine the dynamical processes of grain growth and phase transformation for different binary ordered structures, including the formation of various types of topological defects during the system evolution. Importantly, varying the length scale ratio between the two sublattices allows us to access and predict a much broader range of complex ordered (or quasicrystalline) patterns and superlattices, with results depending on the integer versus noninteger type of ratio and the choice of densities of the two components.

II. MODEL DERIVATION

The PFC equations for the binary AB system can be derived from classical dynamic density functional theory (DDFT), following the procedure described in Ref. [23]. In classical DFT, the free-energy functional for a two-component system is expanded as (see, e.g., Ref. [35])

$$
F/k_B T = \int d\mathbf{r} \sum_i \left[\rho_i \ln \left(\rho_i / \rho_l^i \right) - \delta \rho_i \right] - \sum_{n=2}^{\infty} \frac{1}{n!} \int d\mathbf{r}_1 \cdots d\mathbf{r}_n
$$
$$
\times \sum_{i,\ldots,j} C_{i,\ldots,j}^{(n)}(\mathbf{r}_1, \ldots, \mathbf{r}_n) \delta \rho_i(\mathbf{r}_1) \cdots \delta \rho_j(\mathbf{r}_n), \quad (1)
$$

where $\delta \rho_i = \rho_i - \rho_l^i$, $\rho_{i=A,B}$ is the local atomic number density of the A, B component, ρ_l^i is a reference-state density of the i component, and $C_{i,\ldots,j}^{(n)}$ is the n-point direct correlation function between $i, \ldots, j = A, B$. The dynamics of density fields is governed by the DDFT equations [23,36,37]

$$
\partial \rho_A / \partial t = \nabla \cdot \left(M_A \rho_A \nabla \frac{\delta F}{\delta \rho_A} + \sqrt{\rho_A} \boldsymbol{\eta}_A \right),
$$
$$
\partial \rho_B / \partial t = \nabla \cdot \left(M_B \rho_B \nabla \frac{\delta F}{\delta \rho_B} + \sqrt{\rho_B} \boldsymbol{\eta}_B \right), \quad (2)
$$

where $M_{A(B)}$ is the mobility of the $A(B)$ component and $\boldsymbol{\eta}_{A(B)}$ is the noise field. In principle, the free energy in classical DFT contains all the effects including noise, since the DFT derivation comes from the partition function summing over all states at some finite temperature, and the resulting equilibrium F is a functional of noise-averaged densities (i.e., after ensemble average). Adding an extra noise term in DDFT would then result in a double counting of fluctuations [36]. From a more pragmatic point of view, however, DDFT without fluctuations misses some key dynamic processes, such as nucleation events. In practice, the free-energy functional used and the corresponding density fields are usually

coarse-grained, for which the governing DDFT equations should be stochastic as demonstrated in Ref. [38]. Therefore, for completeness noise is incorporated in the above dynamic equations, where F should then be considered as an effective, coarse-grained free-energy functional but not the true free energy.

Defining the density variation fields $n_A = (\rho_A - \rho_l^A)/\rho_l$ and $n_B = (\rho_B - \rho_l^B)/\rho_l$ (with $\rho_l = \rho_l^A + \rho_l^B$), keeping only two- and three-point direct correlations $C_{ij}^{(2)}(\mathbf{r}_1, \mathbf{r}_2)$ and $C_{ijk}^{(3)}(\mathbf{r}_1, \mathbf{r}_2, \mathbf{r}_3)$ $(i, j, k = A, B)$, and expanding them in Fourier space (with wave number q) via

$$
\hat{C}_{ij}^{(2)}(q) = -\hat{C}_0^{ij} + \hat{C}_2^{ij} q^2 - \hat{C}_4^{ij} q^4 + \cdots ,
$$
$$
\hat{C}_{ijk}^{(3)}(\boldsymbol{q}, \boldsymbol{q}') \simeq \hat{C}_{ijk}^{(3)}(\boldsymbol{q} = \boldsymbol{q}' = 0) = -\hat{C}_0^{ijk}, \quad (3)
$$

we can rewrite Eq. (1) as

$$
\frac{\Delta F}{\rho_l k_B T} = \int d\mathbf{r} \Bigg\{ \Delta \rho_l^A \left(1 + \frac{n_A}{\Delta \rho_l^A} \right) \ln \left(1 + \frac{n_A}{\Delta \rho_l^A} \right) - n_A
$$
$$
+ \Delta \rho_l^B \left(1 + \frac{n_B}{\Delta \rho_l^B} \right) \ln \left(1 + \frac{n_B}{\Delta \rho_l^B} \right) - n_B
$$
$$
+ \frac{\rho_l}{2} \left[\hat{C}_0^{AA} n_A^2 + n_A \left(\hat{C}_2^{AA} \nabla^2 + \hat{C}_4^{AA} \nabla^4 \right) n_A \right.
$$
$$
+ \hat{C}_0^{BB} n_B^2 + n_B \left(\hat{C}_2^{BB} \nabla^2 + \hat{C}_4^{BB} \nabla^4 \right) n_B
$$
$$
\left. + 2 \hat{C}_0^{AB} n_A n_B + 2 n_A \left(\hat{C}_2^{AB} \nabla^2 + \hat{C}_4^{AB} \nabla^4 \right) n_B \right]
$$
$$
+ \frac{\rho_l^2}{6} \left[\hat{C}_0^{AAA} n_A^3 + \hat{C}_0^{BBB} n_B^3 \right.
$$
$$
\left. + 3 \hat{C}_0^{AAB} n_A^2 n_B + 3 \hat{C}_0^{ABB} n_A n_B^2 \right] \Bigg\}, \quad (4)
$$

which is the same as Eq. (A1) in the Appendix of Ref. [23], with $\Delta \rho_l^{A(B)} = \rho_l^{A(B)}/\rho_l$. Note that Eqs. (3) and (4) are based on the assumption of only one characteristic length scale for either A or B sublattice (as determined by $\hat{C}_{ij}^{(2)}$), and the approximation of $\hat{C}_{ijk}^{(3)}$ only by its zero-wave-vector component as used in previous classical DFT work for hard-spheres [39] and Lennard-Jones [40] binary systems.

Substituting Eq. (4) into the DDFT Eqs. (2), choosing the same reference state for A and B, i.e., $\rho_l^A = \rho_l^B$, and keeping only the leading-order terms (via scale analysis), we can derive a new binary PFC model represented by

$$
\partial n_A / \partial t = D_A \nabla^2 \frac{\delta \mathcal{F}}{\delta n_A} + \nabla \cdot \boldsymbol{\eta}_A,
$$
$$
\partial n_B / \partial t = D_B \nabla^2 \frac{\delta \mathcal{F}}{\delta n_B} + \nabla \cdot \boldsymbol{\eta}_B, \quad (5)
$$

where the diffusion coefficients $D_{A(B)} = M_{A(B)} k_B T$, and the resulting PFC free-energy functional is given by

$$
\mathcal{F} = \int d\mathbf{r} \left[\frac{1}{2} \Delta B_A n_A^2 + \frac{1}{2} B_A^x n_A \left(R_A^2 \nabla^2 + 1 \right)^2 n_A \right.
$$
$$
+ \frac{1}{2} \Delta B_B n_B^2 + \frac{1}{2} B_B^x n_B \left(R_B^2 \nabla^2 + 1 \right)^2 n_B
$$
$$
\left. - \frac{1}{3} \tau_A n_A^3 + \frac{1}{4} v_A n_A^4 - \frac{1}{3} \tau_B n_B^3 + \frac{1}{4} v_B n_B^4 \right.
$$

$$+\Delta B_{AB}n_A n_B + B_{AB}^x n_A \left(R_{AB}^2 \nabla^2 + 1\right)^2 n_B$$
$$+\frac{1}{2}w_0 n_A^2 n_B + \frac{1}{2}u_0 n_A n_B^2 \Bigg]. \tag{6}$$

Here $\Delta B_{A(B)} = B_{A(B)}^l - B_{A(B)}^x$, $\Delta B_{AB} = B_{AB}^l - B_{AB}^x$, and all the parameters can be expressed via expansion coefficients of two- and three-point direct correlation functions in Fourier space, i.e.,

$$B_A^x = \frac{\rho_l^A \hat{C}_2^{AA\,2}}{4\hat{C}_4^{AA}}, \quad B_A^l = 1 + \rho_l^A \hat{C}_0^{AA}, \quad R_A = \sqrt{\frac{2\hat{C}_4^{AA}}{\hat{C}_2^{AA}}},$$

$$\tau_A = -\frac{\rho_l}{2}\left(\hat{C}_0^{AA} + \rho_l^A \hat{C}_0^{AAA}\right), \quad v_A = \frac{\rho_l^2}{3}\hat{C}_0^{AAA},$$

$$B_B^x = \frac{\rho_l^B \hat{C}_2^{BB\,2}}{4\hat{C}_4^{BB}}, \quad B_B^l = 1 + \rho_l^B \hat{C}_0^{BB}, \quad R_B = \sqrt{\frac{2\hat{C}_4^{BB}}{\hat{C}_2^{BB}}},$$

$$\tau_B = -\frac{\rho_l}{2}\left(\hat{C}_0^{BB} + \rho_l^B \hat{C}_0^{BBB}\right), \quad v_B = \frac{\rho_l^2}{3}\hat{C}_0^{BBB},$$

$$B_{AB}^x = \frac{\rho_l^A \hat{C}_2^{AB\,2}}{4\hat{C}_4^{AB}}, \quad B_{AB}^l = \rho_l^A \hat{C}_0^{AB}, \quad R_{AB} = \sqrt{\frac{2\hat{C}_4^{AB}}{\hat{C}_2^{AB}}},$$

$$w_0 = \rho_l \rho_l^A \hat{C}_0^{AAB}, \quad u_0 = \rho_l \rho_l^A \hat{C}_0^{ABB}. \tag{7}$$

To reduce the number of parameters, we can rescale the above PFC equations in terms of A parameters, i.e., via a length scale R_A, a time scale $R_A^2/(D_A B_A^x)$, and $n_{A(B)} \to n_{A(B)}\sqrt{v_A/B_A^x}$, leading to

$$\frac{\partial n_A}{\partial t} = \nabla^2 \frac{\delta \mathcal{F}}{\delta n_A} + \boldsymbol{\nabla} \cdot \boldsymbol{\eta}_A, \quad \frac{\partial n_B}{\partial t} = m_B \nabla^2 \frac{\delta \mathcal{F}}{\delta n_B} + \boldsymbol{\nabla} \cdot \boldsymbol{\eta}_B, \tag{8}$$

where $m_B = M_B/M_A$ represents a mobility contrast between A and B species, and the rescaled noise fields satisfy the conditions

$$\langle \boldsymbol{\eta}_A \rangle = \langle \boldsymbol{\eta}_B \rangle = \langle \boldsymbol{\eta}_A \boldsymbol{\eta}_B \rangle = \mathbf{0},$$
$$\left\langle \eta_i^\mu(\boldsymbol{r}, t)\eta_i^\nu(\boldsymbol{r}', t) \right\rangle = 2\Gamma_i k_B T \delta(\boldsymbol{r} - \boldsymbol{r}')\delta(t - t')\delta^{\mu\nu}, \tag{9}$$

with $i = A, B$, $\mu, \nu = x, y$ for a 2D system, and the rescaled noise amplitudes $\Gamma_B/\Gamma_A = M_B/M_A = m_B$. The PFC free-energy functional is rescaled as

$$\mathcal{F} = \int d\boldsymbol{r} \Bigg[-\frac{1}{2}\epsilon_A n_A^2 + \frac{1}{2}n_A \left(\nabla^2 + q_A^2\right)^2 n_A$$
$$-\frac{1}{2}\epsilon_B n_B^2 + \frac{1}{2}\beta_B n_B \left(\nabla^2 + q_B^2\right)^2 n_B$$
$$-\frac{1}{3}g_A n_A^3 + \frac{1}{4}n_A^4 - \frac{1}{3}g_B n_B^3 + \frac{1}{4}v n_B^4$$
$$+\alpha_{AB}n_A n_B + \beta_{AB}n_A \left(\nabla^2 + q_{AB}^2\right)^2 n_B$$
$$+\frac{1}{2}w n_A^2 n_B + \frac{1}{2}u n_A n_B^2 \Bigg], \tag{10}$$

where the dimensionless parameters are given by $q_A = 1$ (due to rescaling), $q_B = R_A/R_B$, $q_{AB} = R_A/R_{AB}$, $\epsilon_{A(B)} = -\Delta B_{A(B)}/B_A^x = (B_{A(B)}^x - B_{A(B)}^l)/B_A^x$, $\alpha_{AB} = \Delta B_{AB}/B_A^x$, $\beta_{AB} = B_{AB}^x/(B_A^x q_{AB}^4)$, $\beta_B = B_B^x/(B_A^x q_B^4)$, $g_{A(B)} = \tau_{A(B)}/\sqrt{B_A^x v_A}$, $v = v_B/v_A$, $w = w_0/\sqrt{B_A^x v_A}$, and $u = u_0/\sqrt{B_A^x v_A}$.
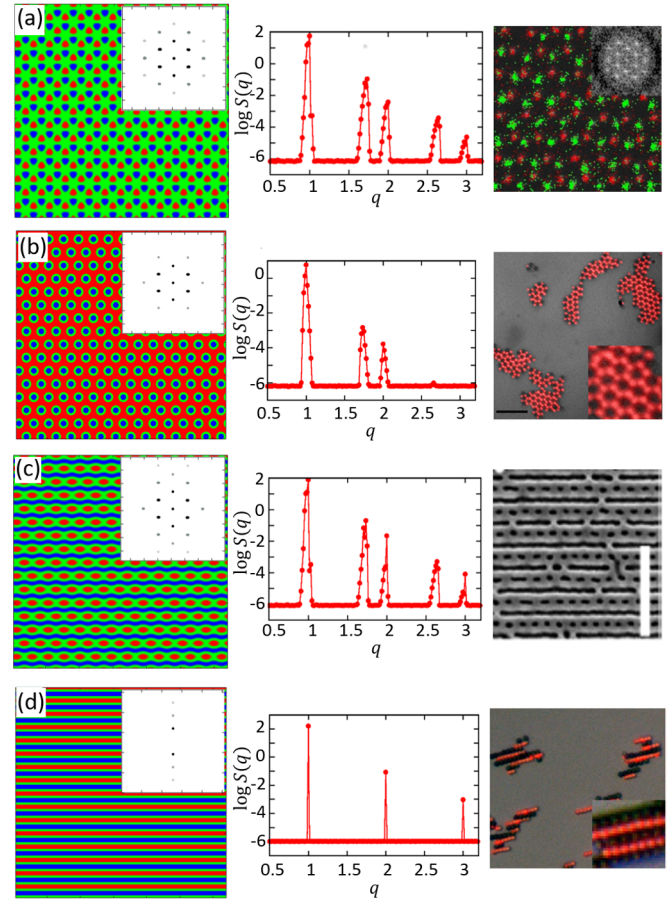

FIG. 1. Some ordered phases obtained from PFC simulations for the case of equal sublattice length scales ($q_A = q_B = 1$), including (a) binary honeycomb (BH), (b) triangular B and honeycomb A (TBHA), (c) elongated triangular A and stripe B (ETASB), and (d) binary stripe (BS). For the first-column simulation results, the red locations correspond to the maximum density of component A, while the blue ones correspond to the maximum density of B. The corresponding diffraction patterns are shown as insets, and the circularly averaged structure factors are given in the second column. As a comparison, the third column shows the related results observed in previous experiments, reprinted with permission from Ref. [8] in (a), from Ref. [2] in (b) and (d), and from Ref. [34] in (c).

III. ORDERED STRUCTURES AND PHASE DIAGRAMS: EQUAL LENGTH SCALES

The binary PFC model constructed here [i.e., Eqs. (8)–(10)], although only including one mode for each of the sublattices, can produce a rich variety of ordered structures as well as their coexistence. Detailed results depend on the selection and competition of length scales between the two sublattices. For simplicity, in this section we consider the case of an equal lattice spacing of A and B sublattices and zero mobility contrast, such that $q_A = q_B = q_{AB} = 1$ and $m_B = 1$, and we use the model parameters of $\alpha_{AB} = 0.5$, $\beta_{AB} = 0.02$, $g_A = g_B = 0.5$, $w = u = 0.3$, and $\beta_B = v = 1$. For these parameters, a total of seven stable phases of 2D binary sublattice ordering have been identified, with some structures and the corresponding diffraction patterns and/or circularly averaged structure factors for the density difference $n_A - n_B$ shown in
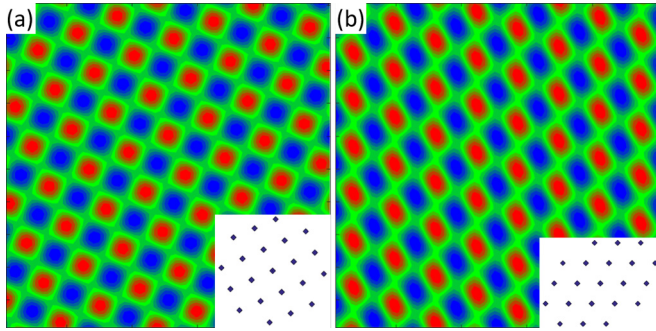
FIG. 2. (a) Binary square (BSq; i.e., checkerboard) and (b) binary rhombic (BR) phases obtained from PFC simulations, with $q_A = q_B = 1$ and positive average densities of A and B components [$n_{A0} = 0.53$, $n_{B0} = 0.82$ for (a) and $n_{A0} = 0.55$, $n_{B0} = 0.80$ for (b)]. The color scheme is the same as that of Fig. 1. Each inset shows the corresponding diffraction pattern.

Figs. 1 and 2. These binary structures or superlattices are basically combinations of triangular, stripe, inverse triangular (noting that an inverse triangular lattice is of honeycomb structure), square, rhombic, and homogeneous states of A and B sublattices, and they are determined by the coupling between n_A and n_B density fields. They include (i) a binary honeycomb (BH) phase with triangular A and B sublattices, (ii) a binary stripe (BS) phase with A and B stripe sublattices, (iii) a combination of elongated triangular A (or B) sublattice and stripe B (or A) sublattice (ETASB or ETBSA), (iv) a pattern with triangular A (B) sublattice but inverse triangular (i.e., honeycomb) structure of B (A) sublattice (TAHB or TBHA), and (v) a binary homogeneous (BHom) state. In addition, two other ordered phases can be found only from the regime of positive average density variations, including (vi) a checkerboard structure shown as binary square (BSq) sublattices of A and B, and (vii) a binary rhombic (BR) phase consisting of A and B rhombic sublattices (see Fig. 2). These seven phases are identified through our numerical simulations of the dynamic Eq. (8), across different ranges of average density values including n_{A0}, n_{B0} varying from -0.5 to 0.5 to obtain phases (i)–(v) and from 0.5 to 1 to obtain phases (vi) and (vii). It is possible that more ordered phases could be found across a broader range of parameter space as a result of the nonlinear coupling between A and B sublattice density fields.

The TAHB (or TBHA) phase has been observed in experiments of 2D binary colloid mixtures [1–3], while the BSq structure has been achieved in both experiments and MC simulations of binary colloidal monolayers [2,19]. The BH phase not only has been obtained in previous experiments of a binary colloidal system with honeycomb symmetry [8], but it also corresponds to the structure of binary 2D hexagonal materials such as hexagonal boron nitride (*h*-BN). The BS structure has also been observed in binary colloids, although the stripe phase obtained in our modeling would be more relevant to that of diblock copolymers given the homogeneous density distribution within each stripe. Although to the best of our knowledge the ETASB (or ETBSA) superlattice has not been found in colloidal systems, a similar phase has been produced in thin-film experiments of binary blends of block

copolymers (controlled by substrate surface prepatterning) [34]. Some of the corresponding experimental images are shown in Fig. 1 for comparison.

A. Phase diagrams: Analytics from one-mode approximation

The corresponding phase diagram of this PFC model can be determined via standard thermodynamics. The phase boundaries for the coexistence between any two phases 1 and 2 are calculated by the conditions

$$\mu_{A1} = \mu_{A2}, \quad \mu_{B1} = \mu_{B2}, \quad \omega_1 = \omega_2, \quad (11)$$

where $\mu_{A(B)} = \partial f / \partial n_{A(B)0}$ is the chemical potential for A (B), with f the free-energy density and $n_{A(B)0}$ the average density variation of A (B) component, and $\omega = f - \mu_A n_{A0} - \mu_B n_{B0}$ is the grand potential density. Given that $\omega = \Omega/V = -P$ with the grand potential Ω, system volume V, and pressure P, Eq. (11) gives the phase coexisting conditions of equal chemical potentials and equal pressure, i.e.,

$$\left.\frac{\partial f}{\partial n_{A0}}\right|_1 (n_{A0_1}, n_{B0_1}) = \left.\frac{\partial f}{\partial n_{A0}}\right|_2 (n_{A0_2}, n_{B0_2}) = \mu_0^A,$$

$$\left.\frac{\partial f}{\partial n_{B0}}\right|_1 (n_{A0_1}, n_{B0_1}) = \left.\frac{\partial f}{\partial n_{B0}}\right|_2 (n_{A0_2}, n_{B0_2}) = \mu_0^B,$$

$$f_1 - \mu_0^A n_{A0_1} - \mu_0^B n_{B0_1} = f_2 - \mu_0^A n_{A0_2} - \mu_0^B n_{B0_2} = -P, \quad (12)$$

where $f_1(n_{A0_1}, n_{B0_1})$ and $f_2(n_{A0_2}, n_{B0_2})$ are the free-energy densities of phases 1 and 2, respectively.

To obtain the free-energy density $f(n_{A0}, n_{B0})$ and the corresponding chemical potentials of A and B components, we use the one-mode approximation for each ordered phase. The corresponding one-mode expressions assumed in our analytic calculations are given in the Appendix. For each binary phase, the parameters in these expressions, including the wave number and amplitudes of the density field, are determined from free-energy minimization [after substituting the one-mode expressions of n_A and n_B into the free-energy functional Eq. (10) and integrating over a unit cell]; from this we then derive the free-energy density $f(n_{A0}, n_{B0})$ for each phase. Results for the example of BH phase are presented in the Appendix.

The resulting phase diagram is multidimensional, e.g., in the ϵ_A-ϵ_B-n_{A0}-n_{B0} parameter space (with all the other model parameters fixed). For simplicity, here we consider the A/B symmetric case of $\epsilon_A = \epsilon_B = \epsilon$, leading to a 3D ϵ-n_{A0}-n_{B0} phase diagram. It would be convenient to calculate the diagrams in two steps: First identify the stability diagram showing the phase of lowest free energy in each regime of the parameter space, with phase boundaries determined by the solution of $f_1(n_{A0}, n_{B0}) = f_2(n_{A0}, n_{B0})$ for any two phases 1 and 2, and then construct the corresponding phase diagrams (showing coexistence between two or three phases) based on Eq. (12). Two sample diagrams at $\epsilon = 0.1$ and 0.3 obtained from our analytic calculations are shown in Figs. 3(a) and 3(b).

B. Phase diagrams: Direct numerical calculations

We also calculate the phase diagrams through direct numerical simulations of this binary PFC model. The dynamic
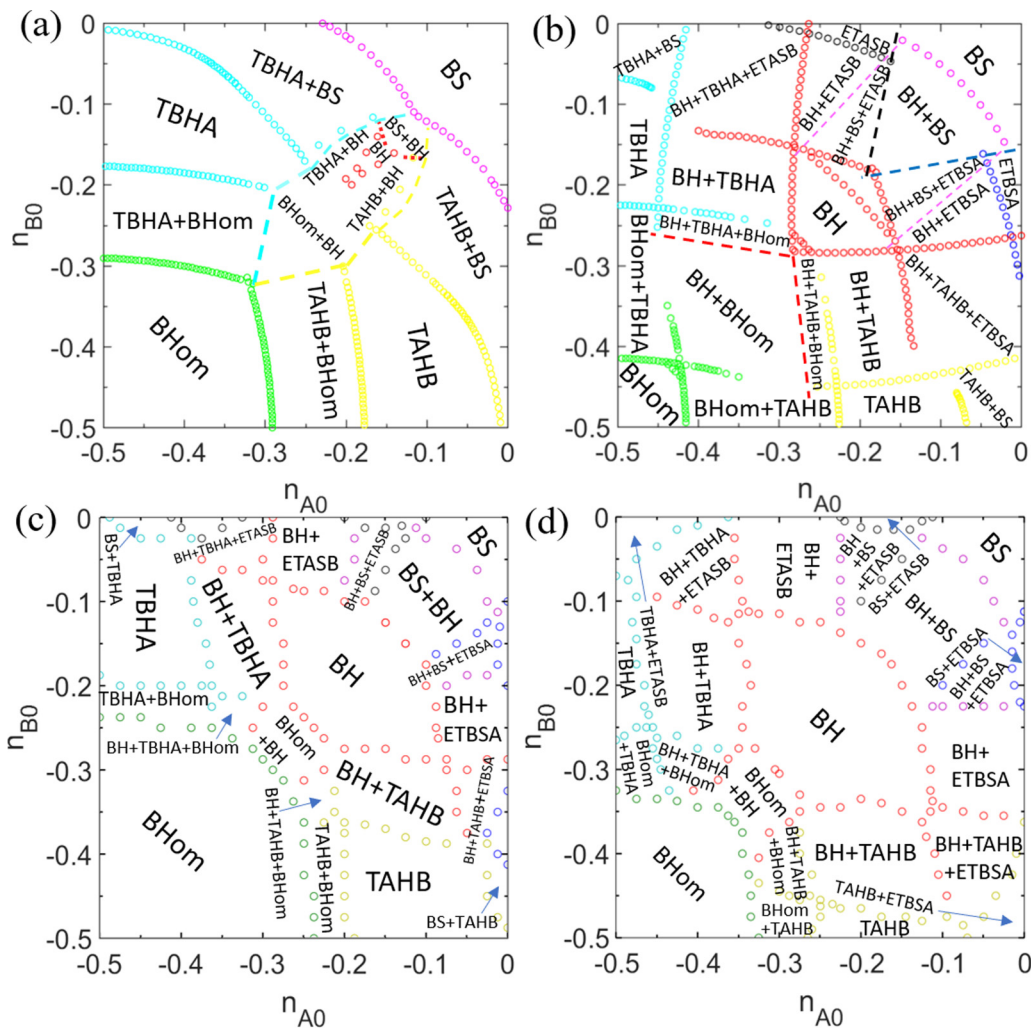
FIG. 3. Phase diagrams of the binary PFC model in the cross-section plane of n_{A0} vs n_{B0} (for n_{A0}, $n_{B0} < 0$) for the case of equal sublattice length scales $q_A = q_B = 1$ at $\epsilon_A = \epsilon_B = 0.1$ [(a) and (c)] and 0.3 [(b) and (d)]. Results of the analytic calculations are shown in (a) and (b), while those determined by direct numerical simulations are given in (c) and (d).

model equation (8) is solved numerically in the absence of noise terms, starting from random initial conditions across the parameter space of (n_{A0}, n_{B0}) at each specific value of $\epsilon = \epsilon_A = \epsilon_B$. The corresponding phase at each point of the parameter space is determined by its steady-state structure. Two of these numerically determined phase diagrams for $\epsilon = 0.1$ and 0.3 are given in Figs. 3(c) and 3(d), respectively, showing some quantitatively different results of phase boundaries as compared to those in Figs. 3(a) and 3(b) obtained from the above analytic calculations. One of the obvious differences is the much larger regime of BH phase identified from numerical solutions. In addition, in Fig. 3(a) with $\epsilon = 0.1$ only two-phase coexistence is obtained from the analytic results under the one-mode approximation, whereas both two- and three-phase coexistence regions are seen in Fig. 3(b) when $\epsilon = 0.3$. This differs from the simulation results in Figs. 3(c) and 3(d), which show two- and three-phase coexistence regions for both values of ϵ.

These differences can be attributed to the oversimplified assumptions in the one-mode expressions of density fields used in the analytic calculations. Generally

the A and B density variation fields are expanded as $n_A = n_{A0} + \sum_j A_j \exp[i(\boldsymbol{q}_{A_j} \cdot \boldsymbol{r} + \varphi_{A_j})] + \text{c.c.}$ and $n_B = n_{B0} + \sum_j B_j \exp[i(\boldsymbol{q}_{B_j} \cdot \boldsymbol{r} + \varphi_{B_j})] + \text{c.c.}$. In the standard procedure of phase diagram calculation that is followed above in Sec. III A, the amplitudes A_j and B_j are assumed to be real once the wave vectors $\boldsymbol{q}_{A_j}$, $\boldsymbol{q}_{B_j}$ and phase shifts φ_{A_j}, φ_{B_j} are identified from the structural symmetry (as given in the Appendix). This procedure has worked well for the previous single-component and alloy PFC models [21,22,30,31]. However, the discrepancies shown in Fig. 3 between analytic results and numerical solutions indicate a more complicated scenario for the case of binary sublattice ordering examined here, particularly regarding the selection of complex phases of A and B amplitudes. More details for the example of BH structure, including the corresponding amplitude equations and phase selection, will be presented elsewhere.

IV. PHASE TRANSFORMATION, GRAIN NUCLEATION, AND GROWTH

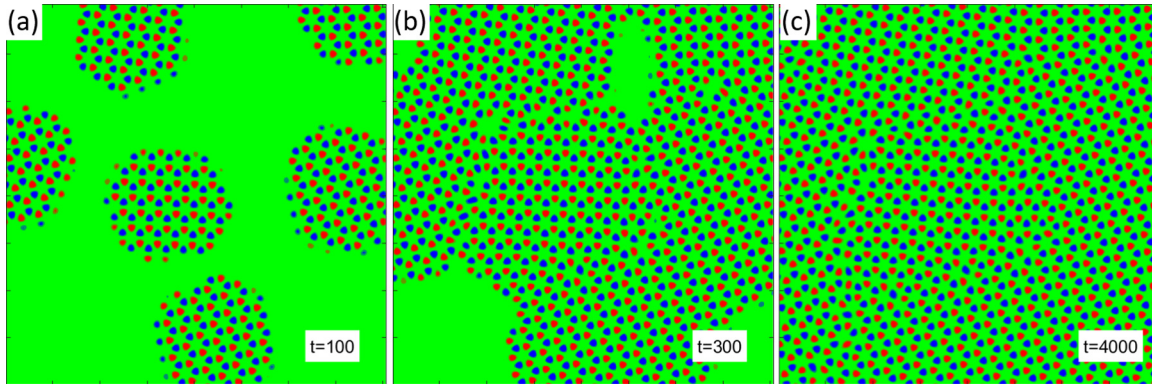Below the melting point, crystallites can nucleate homogeneously or heterogeneously from the supersaturated

FIG. 4. Grain growth and coalescence process obtained from PFC simulation. The nuclei of BH structure grow and impinge to form grain boundaries and a polycrystalline system, with a portion of the simulation results shown at (a) $t = 100$, (b) $t = 300$, and (c) $t = 4000$.

homogeneous state. In either case, those nuclei will grow individually until they merge, which usually leads to the formation of topological defects such as dislocations and grain boundaries in the system. Many factors (e.g., temperature and average densities) determine the ordered structures and dynamics arising from those nucleation processes. The emergence of multiple coexisting phases and the structural transformation between them can also occur during the system evolution due to the phase coexistence determined in the phase diagram. We have conducted a series of simulations to examine this nucleation or phase transformation process, with some sample results given below. Here the nonconserved dynamics is used, for a better control of the grain growth rate and the condition of constant flux, i.e.,

$$\frac{\partial n_A}{\partial t} = -\frac{\delta \mathcal{F}}{\delta n_A} + \mu_A,$$

$$\frac{\partial n_B}{\partial t} = -m_B \left(\frac{\delta \mathcal{F}}{\delta n_B} - \mu_B \right), \qquad (13)$$

where $\mu_{A(B)}$ is the chemical potential of A (B) component. The process of grain growth is controlled through tuning the values of μ_A and μ_B, which emulate the constant flux condition. No noise terms are added in the above PFC dynamic equations used in our simulations, given the nature of heterogeneous nucleation studied here for which noise does not play a crucial role.

A. Nucleation and growth of BH grains

We first study an example of the emergence of binary honeycomb (BH) phase from a homogeneous (BHom) state, simulating the dynamic process of grain nucleation, individual grain growth, grain coalescence, and eventually the formation of a polycrystalline state. Initially 20 circular nuclei of BH structure are placed at random locations in a simulation box, with randomly assigned different orientations. The nuclei evolve and grow individually until the grains merge and form a binary honeycomb film. The average densities for BH and BHom states are set as $n_{A0} = n_{B0} = -0.27$ and -0.47, respectively. The chemical potential $\mu_A = \mu_B$ is set to be -0.58, slightly larger than the corresponding two-phase coexistence value. A portion of the simulation box is shown in Fig. 4,

giving three snapshots during the system evolution. Figure 4(a) shows the early growth stage of individual grains before they impinge on each other, where the process of faceting occurs on the surface of each BH grain which evolves to a hexagon shape. At a later time stage [Fig. 4(b)] the impingement of grains has occurred and coalescence is taking place, which leads to the formation of dislocations and grain boundaries. For both stages, the solidification process is not yet complete and there is still part of the system that is in the homogeneous state. At large enough time the whole system evolves to the ordered state of BH symmetry, as shown in Fig. 4(c). The system is polycrystalline, with grain boundaries separating grains of different orientations.

B. BH-to-BS phase transformation

An example of phase transformation is presented in Fig. 5, showing the dynamic process of transformation from a binary honeycomb (BH) structure to the binary stripe (BS) phase. We use a setup similar to the previous section by initializing 20 BS nuclei at random locations and orientations in coexistence with the BH matrix. The average densities for BH and BS states are set as $n_{A0} = n_{B0} = -0.21$ and -0.0739, respectively, and the system chemical potential is chosen as $\mu_A = \mu_B = -0.35$ (above the corresponding coexistence value). Three snapshots representing different stages of system evolution are given in Fig. 5, exhibiting BH-BS structural transformation as a result of the grain growth of BS nuclei and the subsequent grain coalescence. The individual grain growth rate appears to depend on the initial orientation. Each single stripe of type A or B grows and connects with the neighboring particles of the same type. The growth direction of the binary stripes is not restricted to that of the initial grain, and the fronts could change direction (i.e., curve) during growth. When the differently oriented grains coalesce, some topological defects are formed, including disclinations, dislocations, and grain boundaries, as indicated in the white dashed boxes of Fig. 5(c).

C. BH-to-ETASB phase transformation

Figure 6 presents another example of phase transformation, from the BH to elongated triangular A and stripe B (ETASB)
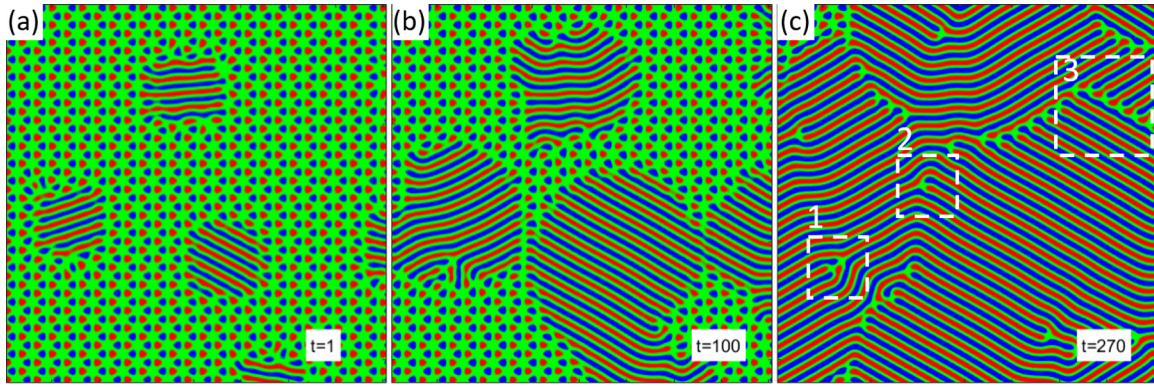
FIG. 5. Binary honeycomb (BH) to binary stripe (BS) phase transformation obtained from PFC simulation. The system transforms from BH to BS phase as a result of growth and merging of individual BS grains, with a portion of the simulation results shown at (a) $t = 1$, (b) $t = 100$, and (c) $t = 270$. Sample defects of disclination, dislocation, and grain boundary are indicated in the white dashed boxes with labels 1, 2, and 3, respectively.

phase. The initial setup here is the same as before, other than the nuclei being of ETASB type as seen in Fig. 6(a). The parameters used in the simulation are $n_{A0} = -0.33$ and $n_{B0} = -0.1427$ for the BH matrix, $n_{A0} = -0.3417$ and $n_{B0} = 0.002$ for the ETASB nuclei, $\mu_A = -0.6302$, and $\mu_B = -0.3225$. During the system evolution, the BH structure transforms into ETASB starting at the edges of the growing grain. As seen in Figs. 6(b) and 6(c), in this case type B particles transform from a spatial arrangement of triangular symmetry to stripe. To accommodate this transformation, type A particle densities transform from a structure of triangular symmetry to elongated triangular symmetry. If the initial ETASB grain orientation is around or less than $5°$ with respect to the direction of the surrounding matrix, then the grain rotates to match the orientation of the matrix. For larger grain orientations, step defects or kinks are formed. This kink defect acts as a transition between two different orientations of the merging grains. An example is enclosed by the dashed box in Fig. 6(c) where the whole system has been transformed to a defected ETASB state.

V. ORDERED BINARY STRUCTURES WITH COMPETING LENGTH SCALES

Two of the key factors controlling the ordering of BiCCs are (i) the coupling and competition among different length scales, and (ii) the average density variations of A and B components. The effect of different length scales can be modeled via changing the ratio between q_A and q_B in the PFC free-energy functional [Eq. (10)], i.e., the characteristic wave numbers of the two sublattices. We then simulate the emergence of the corresponding BiCC structures from the initial supersaturated homogeneous state for various values of average density variations n_{A0} and n_{B0}. The system dynamics is governed by Eq. (8). Some of the predicted binary ordered structures for two different q_B/q_A ratios are shown in Figs. 7 and 8, as identified from our numerical simulations. In all cases, the model parameters are chosen as $\epsilon_A = \epsilon_B = 0.1$, $q_A = 1$, $m_B = 1$, $\alpha_{AB} = 0.5$, $\beta_{AB} = 0$, $g_A = g_B = 0.5$, $w = u = 0.3$, and $\beta_B = v = 1$.

Results for the length scale ratio $q_B/q_A = 2$ are given in Fig. 7, where the first two columns show the spatial
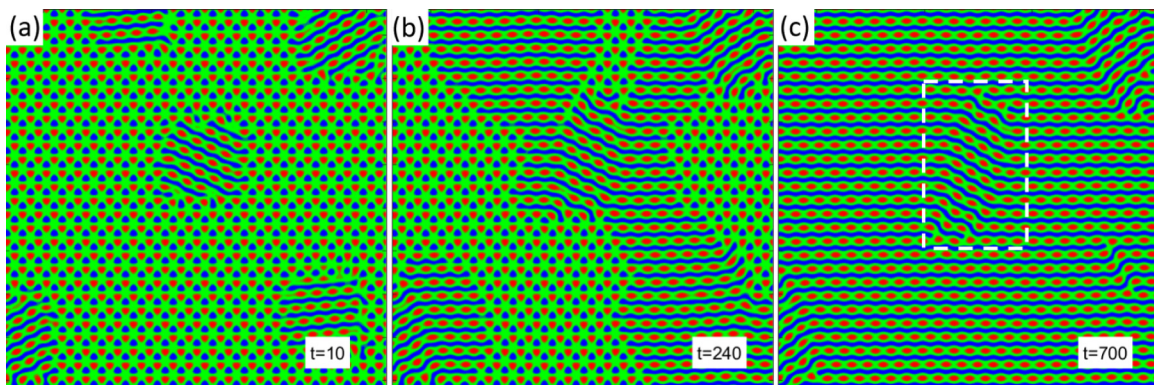

FIG. 6. Binary honeycomb (BH) to elongated triangular A and stripe B (ETASB) phase transformation obtained from PFC simulation. Snapshots of the time evolution of a portion of the simulated system are shown at (a) $t = 10$, (b) $t = 240$, and (c) $t = 700$. A region of kink defects is indicated in (c).
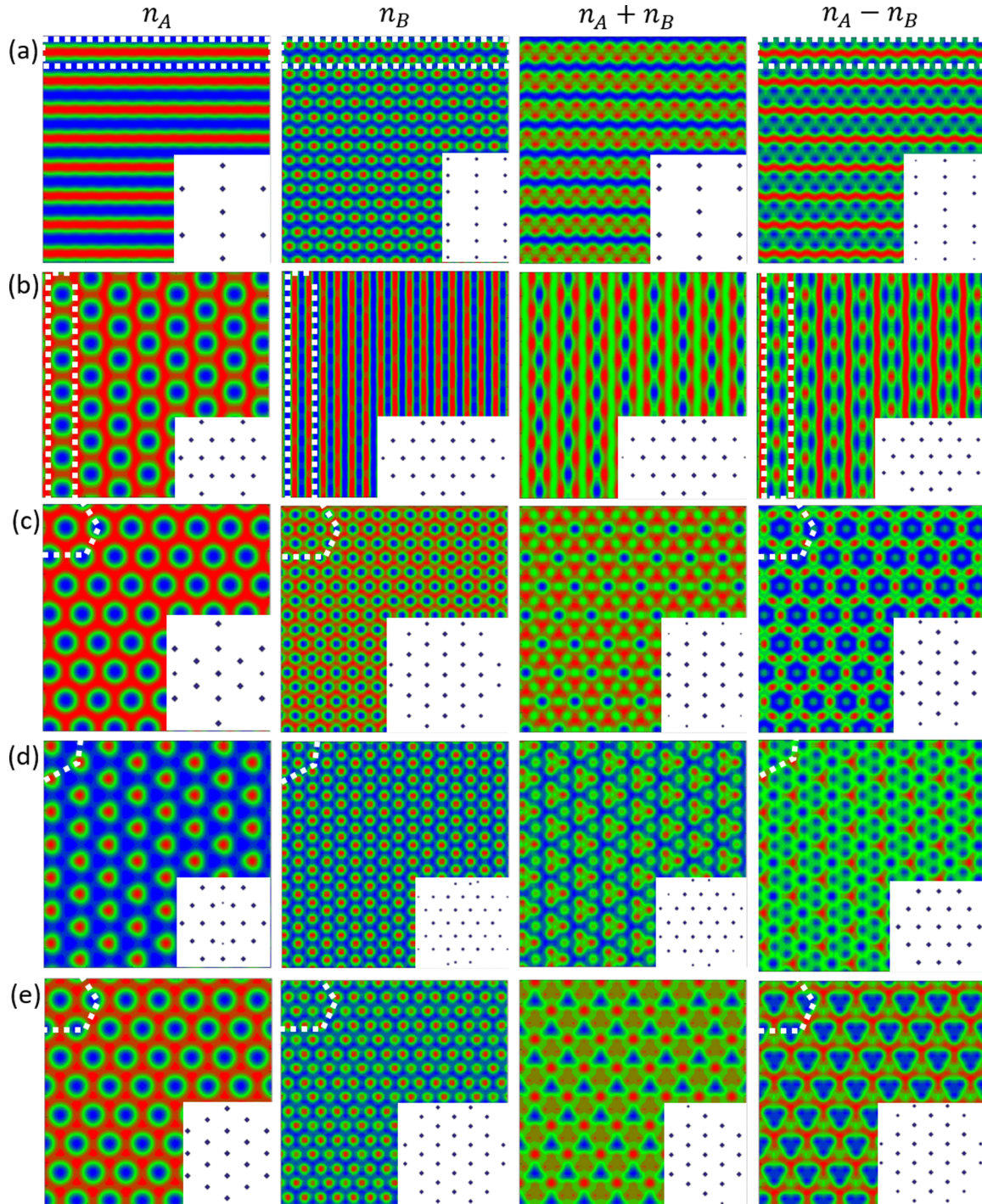
FIG. 7. Some binary ordered structures predicted by PFC simulation, for $q_A = 1$ and $q_B = 2$, and (a) $n_{A0} = 0.05$ and $n_{B0} = -0.1$, (b) $n_{A0} = 0.35$ and $n_{B0} = 0.25$, (c) $n_{A0} = 0.25$ and $n_{B0} = 0.4$, (d) $n_{A0} = -0.15$ and $n_{B0} = -0.1$, and (e) $n_{A0} = 0.3$ and $n_{B0} = -0.1$. The first three columns show the spatial distributions of densities n_A, n_B, and $n_A + n_B$, respectively, where red represents the density maximum and blue represents the density minimum. The fourth column is for the density difference $n_A - n_B$, with red representing the density maximum of A component and blue representing the density maximum of B component. The diffraction patterns of the corresponding density field are shown in the insets.

distributions of density fields for each type of particle, i.e., n_A in the first column and n_B in the second column, and the third column shows the total density field $n_A + n_B$. In these three columns, the red regions correspond to the maxima of the corresponding density field, and the blue regions represent the minima. Column four presents the density difference

$n_A - n_B$, giving the locations of the density maximum for both A component (red) and B component (blue). It is a better representation of the overall pattern and the A/B coupling as compared to $n_A + n_B$. Five examples given in this figure [panels (a)–(e) in Fig. 7] are obtained from different combinations of average densities n_{A0} and n_{B0}. The individual sublattice
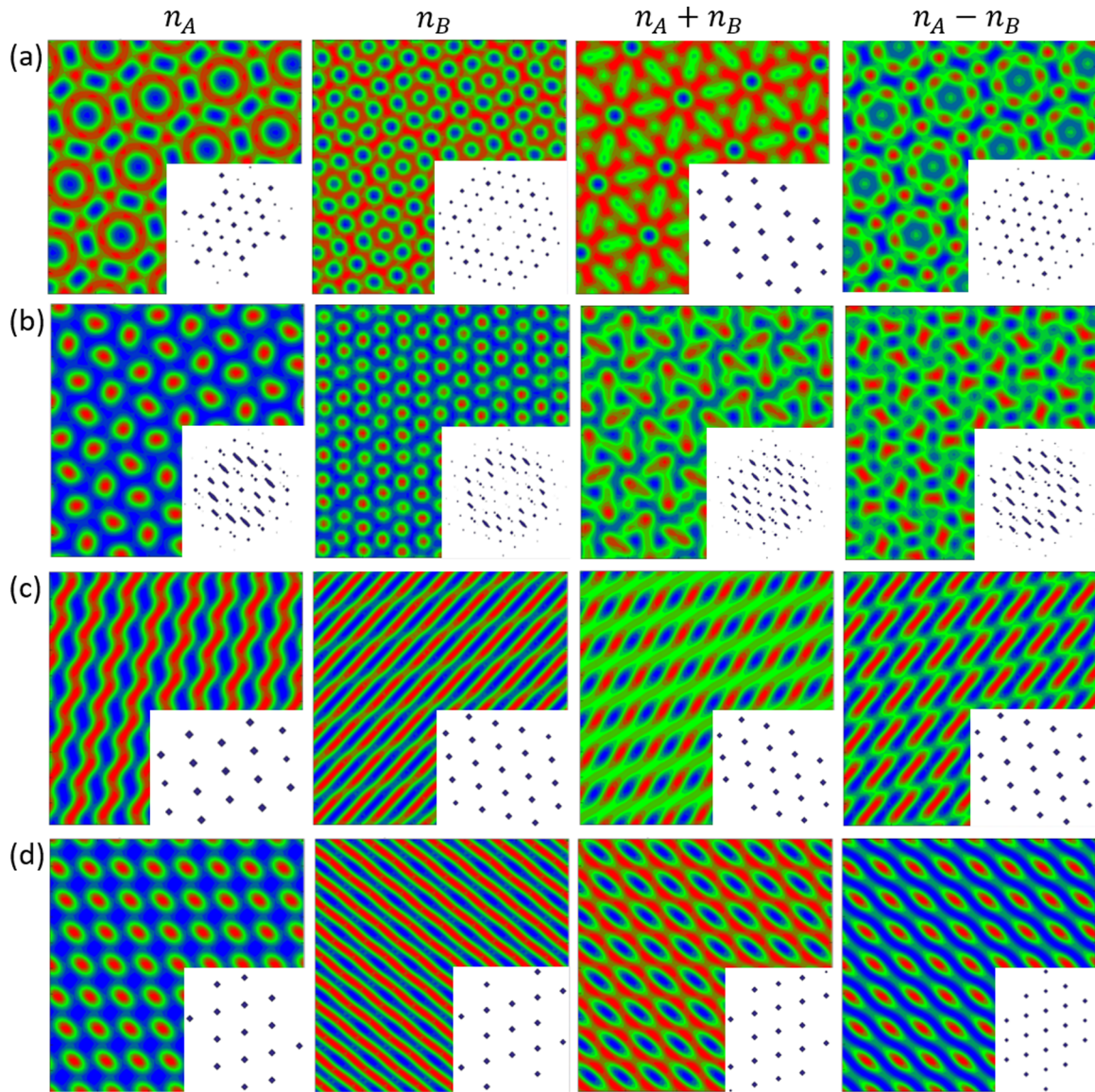
FIG. 8. Some binary ordered structures predicted by PFC simulation, for $q_A = 1$ and $q_B = 1.62$, and (a) $n_{A0} = 0.40$ and $n_{B0} = 0.40$, (b) $n_{A0} = -0.05$ and $n_{B0} = -0.15$, (c) $n_{A0} = 0.25$ and $n_{B0} = 0.25$, and (d) $n_{A0} = 0.05$ and $n_{B0} = 0.2$. The color scheme and the arrangement of columns are the same as that of Fig. 7.

structures for n_A and n_B are of triangular, honeycomb, or stripe type, although additional peaks appear in their diffraction patterns as compared to the corresponding standard lattice structures, which can be attributed to the coupling between the two density fields and the two sublattices.

In Fig. 7(a), n_A is shown as a modified stripe phase and n_B as a modified triangular phase with a smaller length scale (given that $q_B/q_A = 2$). The positions of n_A maxima overlay with those of n_B minimum, and for one structural unit every two rows of n_B maxima correspond to one row of n_A maxima without any overlaps, as indicated by the white dashed boxes in the first two columns of Fig. 7(a). The corresponding super-imposed structure is highlighted by a dashed box in the fourth column representing the density difference $n_A - n_B$. Similar correspondence between the locations of A and B components can be found in other types of ordered structures or super-lattices. In Fig. 7(b), the n_A and n_B distributions are shown

as a modified honeycomb and a modified strip structure, respectively, and every two arrays of n_B maxima correspond to one array of n_A minima (see the enclosed regions of white dashed boxes inside). Figure 7(c) gives an example in which both n_A and n_B are of a honeycomb pattern. In this case, each B honeycomb is enclosed by a larger honeycomb ring of A component, as can be seen more clearly from the structural unit highlighted by the white boxes. In Fig. 7(d), both n_A and n_B are of modified triangular phase, with a smaller lattice spacing for the B sublattice. In the overall pattern of $n_A - n_B$, A particles appear as red forming a large-spacing triangular structure, while B particles (blue) occupy in between, shown as a small-spacing triangular pattern. The case of honeycomb A and triangular B sublattice structures is given in Fig. 7(e). Each unit of the overall binary pattern is featured by a large honeycomb ring of A component enclosing a smaller triangle composed of three B particles.
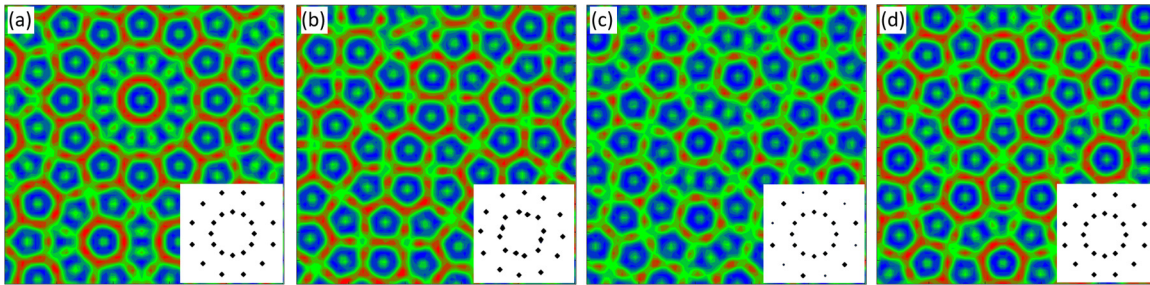
FIG. 9. Sample quasicrystalline patterns obtained from PFC simulation, for $q_A = 1$ and $q_B = (\sqrt{2} + \sqrt{6})/2$, and (a) $n_{A0} = 0.25$ and $n_{B0} = 0.33$, (b) $n_{A0} = 0.28$ and $n_{B0} = 0.3$, (c) $n_{A0} = 0.27$ and $n_{B0} = 0.37$, and (d) $n_{A0} = 0.3$ and $n_{B0} = 0.3$. The structure for density difference $n_A - n_B$ and the corresponding diffraction pattern are shown in each panel.

More complicated binary ordered (or quasiordered) structures can be obtained when the length scale ratio q_B/q_A is not an integer. Some sample results are shown in Fig. 8 for $q_B/q_A = 1.62$. We use similar ways of representing individual and total density fields and density difference in four columns of the figure, with the same color scheme for spatial density distribution as above. Since the B sublattice is of a smaller length scale, each of its clusterlike structural units can be enclosed inside a larger-scale A unit, as seen in Fig. 8(a). On the other hand, the B particles can also distribute in an orderly fashion within the large spacing of elongated A particles, such as the example of Fig. 8(b). Another possibility is the alternating ordered arrangement of A and B particle clusters, which forms a superlattice as shown in Figs. 8(c) and 8(d).

Interestingly, when the sublattice length ratio q_B/q_A is irrational and equal to the characteristic length scale ratio for quasicrystals, e.g., $q_B/q_A = 2\cos(\pi/12) = (\sqrt{2} + \sqrt{6})/2$ for 12-fold symmetry, the corresponding quasicrystalline structures are expected to emerge, similar to the case of single-component quasicrystals found in the two-mode PFC modeling [33]. We have obtained some stable quasicrystalline patterns with binary sublattices through spot checks of simulation outcomes (both structures and diffraction patterns), with some sample results given in Fig. 9. It should be cautioned that the quasicrystalline structures presented here are actually strained due to the periodic boundary conditions applied, and more systematic study is needed to further investigate them.

VI. CONCLUSIONS

We have derived a binary PFC model with sublattice ordering based on the classical dynamic DFT for two-component systems. The model is applied to the study of binary colloidal crystals, including phase ordering and structural transformations. Through the control of length scale contrast and coupling between two sublattices and the tuning of average densities of A and B components, a wide variety of ordered (or quasicrystalline) structures and superlattices have been generated from the model. For the simplest case of equal sublattice length scales, we identify seven binary phases, and calculate the corresponding phase diagrams (in the range of negative average density variations) both analytically and numerically. Much richer phenomena of binary phase ordering are obtained and predicted for different length scales of A and B sublattices, which could be the combination of two regular sublattice ordered structures when the length scale ratio is an integer,

or could appear as more complex patterns or motifs when the ratio is a noninteger.

The dynamic processes of system evolution and transformation have also been produced in our simulations. These include grain nucleation, growth, coalescence, and the formation of topological defects such as grain boundaries, dislocations, disclinations, and kinks or steps, as demonstrated in the examples of BH grain growth from a homogeneous state and structural transformation between two ordered phases (e.g., from BH to BS phase and from BH to ETASB structure) examined here. Our PFC modeling approach and the underlying mechanisms of scale coupling and competition are of a generic nature, and thus can be straightforwardly extended to the systematic study of different kinds of binary colloidal crystals including more varieties of binary phases in both two and three dimensions as well as their ordering and transformation dynamics.

APPENDIX: ONE-MODE APPROXIMATION OF BINARY ORDERED PHASES

In the one-mode approximation, the density variation fields n_A and n_B for various binary 2D ordered phases can be represented by the following: (i) For the binary honeycomb (BH) phase, due to the triangular ordering of A and B sublattices that are shifted by $\boldsymbol{\delta} = a\hat{y} = (4\pi/3q)\hat{y}$ with respect to each other, we have

$$n_A = n_{A0} + \sum_{j=1}^{3} A_j e^{i\boldsymbol{q}_j \cdot \boldsymbol{r}} + \text{c.c.}$$
$$= n_{A0} + 2A_0[2\cos(\sqrt{3}qx/2)\cos(qy/2) + \cos(qy)],$$
$$n_B = n_{B0} + \sum_{j=1}^{3} B_j e^{i\boldsymbol{q}_j \cdot (\boldsymbol{r}+\boldsymbol{\delta})} + \text{c.c.}$$
$$= n_{B0} + 2B_0[2\cos(\sqrt{3}qx/2)\cos(qy/2 + 2\pi/3) + \cos(qy + 4\pi/3)]. \tag{A1}$$

(ii) For the phase of binary stripe (BS), the antiphase of A versus B field leads to

$$n_A = n_{A0} + A_0(e^{iqy} + \text{c.c.}) = n_{A0} + 2A_0\cos(qy),$$

$$n_B = n_{B0} + B_0[e^{i(qy+\pi)} + \text{c.c.}] = n_{B0} - 2B_0\cos(qy). \quad (A2)$$

(iii) For the elongated triangular A and stripe B (ETASB) phase, we assume

$$n_A = n_{A0} + 4A_0[\cos(\sqrt{3}qx/2)\cos(qy/2) + \cos(qy)],$$

$$n_B = n_{B0} + 2B_0\cos(qy + 4\pi/3). \quad (A3)$$

(iv) The one-mode expression for the phase of triangular A and honeycomb B (TAHB) is given by

$$n_A = n_{A0} + 2A_0[2\cos(\sqrt{3}qx/2)\cos(qy/2) + \cos(qy)],$$

$$n_B = n_{B0} - 2B_0[2\cos(\sqrt{3}qx/2)\cos(qy/2) + \cos(qy)]. \quad (A4)$$

The one-mode results for two other variants—ETBSA and TBHA—can be expressed in a similar way.

For the binary honeycomb (BH) phase, substituting the one-mode expression Eq. (A1) into the free-energy functional Eq. (10) and integrating over a cell of ($0 \leqslant x \leqslant \sqrt{3}a$, $0 \leqslant y \leqslant 3a$) with $a = 4\pi/3q$, we obtain the free-energy density as

$$f_{\text{BH}} = f_0 + 3a_1A_0^2 + 3b_1B_0^2 + 4a_2A_0^3 + 4b_2B_0^3 + \frac{45}{2}A_0^4$$

$$+ \frac{45}{2}vB_0^4 - 3cA_0B_0 - 3wA_0^2B_0 - 3uA_0B_0^2, \quad (A5)$$

where

$$f_0 = \tfrac{1}{2}\left(-\epsilon_A + q_A^4\right)n_{A0}^2 + \tfrac{1}{2}\left(-\epsilon_B + \beta_B q_B^4\right)n_{B0}^2$$

$$- \tfrac{1}{3}g_A n_{A0}^3 - \tfrac{1}{3}g_B n_{B0}^3 + \tfrac{1}{4}n_{A0}^4 + \tfrac{1}{4}v n_{B0}^4$$

$$+ \left(\alpha_{AB} + \beta_{AB}q_{AB}^4\right)n_{A0}n_{B0}$$

$$+ \tfrac{1}{2}w n_{A0}^2 n_{B0} + \tfrac{1}{2}u n_{A0}n_{B0}^2, \quad (A6)$$

and

$$a_1 = -\epsilon_A - 2g_A n_{A0} + 3n_{A0}^2 + wn_{B0} + \left(q^2 - q_A^2\right)^2,$$

$$a_2 = -g_A + 3n_{A0},$$

$$b_1 = -\epsilon_B - 2g_B n_{B0} + 3vn_{B0}^2 + un_{A0} + \beta_B\left(q^2 - q_B^2\right)^2,$$

$$b_2 = -g_B + 3vn_{B0},$$

$$c = \alpha_{AB} + wn_{A0} + un_{B0} + \beta_{AB}\left(q^2 - q_{AB}^2\right)^2. \quad (A7)$$

The equilibrium state of this binary honeycomb phase is determined by the minimization of free-energy density in terms of wave number q and amplitudes A_0 and B_0. Minimizing Eq. (A5) with respect to q gives

$$q_{\text{eq}}^2 = \frac{q_A^2 A_0^2 + \beta_B q_B^2 B_0^2 - \beta_{AB}q_{AB}^2 A_0 B_0}{A_0^2 + \beta_B B_0^2 - \beta_{AB}A_0 B_0}. \quad (A8)$$

In the A/B symmetric case we have $A_0 = B_0$ and thus $q_{\text{eq}}^2 = (q_A^2 + \beta_B q_B^2 - \beta_{AB}q_{AB}^2)/(1 + \beta_B - \beta_{AB})$. Here we consider the simplest scenario of $q_A = q_B = q_{AB} = q_0 = 1$; thus $q_{\text{eq}} = q_0 = 1$ for any values of A_0 and B_0, and Eq. (A7) becomes $a_1 = -\epsilon_A - 2g_A n_{A0} + 3n_{A0}^2 + wn_{B0}$, $a_2 = -g_A + 3n_{A0}$, $b_1 = -\epsilon_B - 2g_B n_{B0} + 3vn_{B0}^2 + un_{A0}$, $b_2 = -g_B + 3vn_{B0}$, and $c = \alpha_{AB} + wn_{A0} + un_{B0}$.

Minimizing f_{BH} with respect to amplitudes A_0 and B_0 leads to

$$30A_0^3 + 4a_2A_0^2 + 2a_1A_0 - 2wA_0B_0 - uB_0^2 - cB_0 = 0,$$

$$30vB_0^3 + 4b_2B_0^2 + 2b_1B_0 - 2uA_0B_0 - wA_0^2 - cA_0 = 0. \quad (A9)$$

The equilibrium amplitudes A_0^{eq} and B_0^{eq} are determined by the solution of Eq. (A9) giving the minimum f_{BH}, which will then be used in the calculation of chemical potentials and phase diagrams [see Eq. (12)]. A similar analysis can be conducted for all other phases based on the assumed expressions of the one-mode approximation given above.

[1] C. J. Kiely, J. Fink, M. Brust, D. Bethell, and D. J. Schiffrin, Spontaneous ordering of bimodal ensembles of nanoscopic gold clusters, Nature (London) **396**, 444 (1998).

[2] K. S. Khalil, A. Sagastegui, Y. Li, M. A. Tahir, J. E. S. Socolar, B. J. Wiley, and B. B. Yellen, Binary colloidal structures assembled through ising interactions, Nat. Commun. **3**, 794 (2012).

[3] M. H. Kim, S. H. Im, and O. O. Park, Fabrication and structural analysis of binary colloidal crystals with two-dimensional superlattices, Adv. Mater. **17**, 2501 (2005).

[4] F. X. Redl, K.-S. Cho, C. B. Murray, and S. O'Brien, Three-dimensional binary superlattices of magnetic nanocrystals and semiconductor quantum dots, Nature (London) **423**, 968 (2003).

[5] E. V. Shevchenko, D. V. Talapin, N. A. Kotov, S. O'Brien, and C. B. Murray, Structural diversity in binary nanoparticle superlattices, Nature (London) **439**, 55 (2006).

[6] Z. Cai, Y. J. Liu, X. Lu, and J. Teng, Fabrication of well-ordered binary colloidal crystals with extended size ratios for broadband reflectance, ACS Appl. Mater. Interf. **6**, 10265 (2014).

[7] U. Ognysta, A. Nych, V. Nazarenko, M. Skarabot, and I. Musevic, Design of 2D binary colloidal crystals in a nematic liquid crystal, Langmuir **25**, 12092 (2009).

[8] T. Honold, K. Volk, M. Retsch, and M. Karg, Binary plasmonic honeycomb structures: High-resolution EDX mapping and optical properties, Colloids Surf., A **510**, 198 (2016).

[9] Y. Wan, Z. Cai, L. Xia, L. Wang, Y. Li, Q. Li, and X. Zhao, Simulation and fabrication of binary colloidal photonic crystals and their inverse structures, Mater. Lett. **63**, 2078 (2009).

[10] W. H. Evers, B. D. Nijs, L. Filion, S. Castillo, M. Dijkstra, and D. Vanmaekelbergh, Entropy-driven formation of binary semiconductor-nanocrystal superlattices, Nano Lett. **10**, 4235 (2010).

[11] Z. Chen and S. O'Brien, Structure direction of II-VI semiconductor quantum dot binary nanoparticle superlattices by tuning radius ratio, ACS Nano **2**, 1219 (2008).

[12] P.-Y. Wang, H. Pingle, P. Koegler, H. Thissen, and P. Kingshott, Self-assembled binary colloidal crystal monolayers as cell culture substrates, J. Mater. Chem. B **3**, 2545 (2015).

[13] P.-Y. Wang, S. S.-C. Hung, H. Thissen, P. Kingshott, and R. C.-B. Wong, Binary colloidal crystals (BCCs) as a feeder-free system to generate human induced pluripotent stem cells (hiPSCs), Sci. Rep. **6**, 36845 (2016).

[14] M. A. Kostiainen, P. Hiekkataipale, A. Laiho, V. Lemieux, J. Seitsonen, J. Ruokolainen, and P. Ceci, Electrostatic assembly of binary nanoparticle superlattices using protein cages, Nat. Nanotechnol. **8**, 52 (2013).

[15] M. D. Eldridge, P. A. Madden, and D. Frenkel, Entropy-driven formation of a superlattice in a hard-sphere binary mixture, Nature (London) **365**, 35 (1993).

[16] M. I. Bodnarchuk, M. V. Kovalenko, W. Heiss, and D. V. Talapin, Energetic and entropic contributions to self-assembly of binary nanocrystal superlattices: Temperature as the structure-directing factor, J. Am. Chem. Soc. **132**, 11967 (2010).

[17] K. L. Heatley, F. Ma, and N. Wu, Colloidal molecules assembled from binary spheres under an AC electric field, Soft Matter **13**, 436 (2017).

[18] S. N. Petris, J. Stankovich, D. Y. C. Chan, and R. H. Ottewill, Modeling the structure of charged binary colloidal dispersions, Langmuir **19**, 1121 (2003).

[19] Y. Yang, L. Fu, C. Marcoux, J. E. S. Socolar, P. Charbonneau, and B. B. Yellen, Phase transformations in binary colloidal monolayers, Soft Matter **11**, 2404 (2015).

[20] T. Stirner and J. Sun, Molecular dynamics simulation of the structural configuration of binary colloidal monolayers, Langmuir **21**, 6636 (2005).

[21] K. R. Elder, M. Katakowski, M. Haataja, and M. Grant, Modeling Elasticity in Crystal Growth, Phys. Rev. Lett. **88**, 245701 (2002); K. R. Elder and M. Grant, Modeling elastic and plastic deformations in nonequilibrium processing using phase field crystals, Phys. Rev. E **70**, 051605 (2004).

[22] K. R. Elder, N. Provatas, J. Berry, P. Stefanovic, and M. Grant, Phase field crystal modeling and classical density functional theory of freezing, Phys. Rev. B **75**, 064107 (2007).

[23] Z.-F. Huang, K. R. Elder, and N. Provatas, Phase-field-crystal dynamics for binary systems: Derivation from dynamical density functional theory, amplitude equation formalism, and applications to alloy heterostructures, Phys. Rev. E **82**, 021605 (2010).

[24] Z.-F. Huang and K. R. Elder, Mesoscopic and Microscopic Modeling of Island Formation in Strained Film Epitaxy, Phys. Rev. Lett. **101**, 158701 (2008); Morphological instability, evolution, and scaling in strained epitaxial films: An amplitude-equation analysis of the phase-field-crystal model, Phys. Rev. B **81**, 165421 (2010).

[25] P. Hirvonen, M. M. Ervasti, Z. Fan, M. Jalalvand, M. Seymour, S. M. Vaez Allaei, N. Provatas, A. Harju, K. R. Elder,

and T. Ala-Nissila, Multiscale modeling of polycrystalline graphene: A comparison of structure and defect energies of realistic samples from phase field crystal models, Phys. Rev. B **94**, 035414 (2016).

[26] D. Taha, S. K. Mkhonta, K. R. Elder, and Z.-F. Huang, Grain Boundary Structures and Collective Dynamics of Inversion Domains in Binary Two-Dimensional Materials, Phys. Rev. Lett. **118**, 255501 (2017).

[27] M. Smirman, D. Taha, A. K. Singh, Z.-F. Huang, and K. R. Elder, Influence of misorientation on graphene moiré patterns, Phys. Rev. B **95**, 085407 (2017).

[28] S. van Teeffelen, R. Backofen, A. Voigt, and H. Löwen, Derivation of the phase-field-crystal model for colloidal solidification, Phys. Rev. E **79**, 051404 (2009).

[29] G. Tegze, L. Gránásy, G. I. Tóth, J. F. Douglas, and T. Pusztai, Tuning the structure of non-equilibrium soft materials by varying the thermodynamic driving force for crystal ordering, Soft Matter **7**, 1789 (2011).

[30] M. Greenwood, N. Ofori-Opoku, J. Rottler, and N. Provatas, Modeling structural transformations in binary alloys with phase field crystals, Phys. Rev. B **84**, 064104 (2011).

[31] N. Ofori-Opoku, J. Stolle, Z.-F. Huang, and N. Provatas, Complex order parameter phase-field models derived from structural phase-field-crystal models, Phys. Rev. B **88**, 104106 (2013).

[32] J. Berry, K. R. Elder, and M. Grant, Simulation of an atomistic dynamic field theory for monatomic liquids: Freezing and glass formation, Phys. Rev. E **77**, 061506 (2008).

[33] C. V. Achim, M. Schmiedeberg, and H. Löwen, Growth Modes of Quasicrystals, Phys. Rev. Lett. **112**, 255501 (2014).

[34] A. Stein, G. Wright, K. G. Yager, G. S. Doerk, and C. T. Black, Selective directed self-assembly of coexisting morphologies using block copolymer blends, Nat. Commun. **7**, 12366 (2016).

[35] Y. Singh, Density-functional theory of freezing and properties of the ordered phase, Phys. Rep. **207**, 351 (1991).

[36] U. M. B. Marconi and P. Tarazona, Dynamic density functional theory of fluids, J. Chem. Phys. **110**, 8032 (1999).

[37] A. J. Archer, Dynamical density functional theory: Binary phase-separating colloidal fluid in a cavity, J. Phys.: Condens. Matter **17**, 1405 (2005).

[38] A. J. Archer and M. Rauscher, Dynamical density functional theory for interacting brownian particles: stochastic or deterministic? J. Phys. A **37**, 9325 (2004).

[39] S. J. Smithline and A. D. J. Haymet, Density functional theory for the freezing of 1:1 hard sphere mixtures, J. Chem. Phys. **86**, 6486 (1987).

[40] S. W. Rick and A. D. J. Haymet, Density functional theory for the freezing of Lennard-Jones binary mixtures, J. Chem. Phys. **90**, 1188 (1989).